Journal of Materials Chemistry A

Accepted Manuscript

ROYAL SOCIETY OF CHEMISTRY

www.rsc.org/materialsA

Cite this: DOI: 10.1039/c0xx00000x

www.rsc.org/xxxxxx

Paper

A novel AgPd hollow spheres arched on graphene as an efficient catalyst for the dehydrogenation of formic acid at room temperature

Yiqun Jiang, Xiulin Fan, Xuezhang Xiao, Teng Qin, Liuting Zhang, Fulei Jiang, Meng Li, Shouquan Li, Hongwei Ge, Lixin Chen*

Received (in XXX, XXX) Xth XXXXXXXXX 20XX, Accepted Xth XXXXXXXXX 20XX
DOI: 10.1039/b000000x

Highly dispersed AgPd hollow spheres arched on graphene (denoted as AgPd-Hs/G) were successfully synthesized through a facile one-pot hydrothermal route for the first time. The fabrication strategy was efficient and green by using L-Ascorbic acid (L-AA) as the reductant and trisodium citrate dihydrate as the stabilizer, without employing any seed, surfactant, organic solvent, template, stabilizing agent, or complicated apparatus. The as-synthesized AgPd-Hs/G catalyst exhibits a sphere-shaped hollow structure with an average diameter of about 18 nm and a thin wall of about 5 nm. The hollow architecture with thin wall and the excellent dispersion on the graphene ensure that most of the atoms are located on the surface or sub-surface, which provides reactive catalytic sites for the dehydrogenation of formic acid. Therefore, superior catalytic effect was achieved compared with other catalysts such as Pd/G and AgPd/C. The as-synthesized AgPd-Hs/G exhibits a catalytic activity with an initial turnover frequency (TOF) value of as high as 333 mol H_2 mol^{-1} catalyst h^{-1} even at room temperature (25 ^oC) toward the decomposition of formic acid. The present AgPd-Hs/G with efficient catalysis on the dehydrogenation of formic acid without any CO generation at room temperature can pave the way for the practical liquid hydrogen storage system and therefore promote the application of formic acid on fuel cell systems.

Introduction

Hydrogen, an essential reactant in the chemical industry, is regarded widely as a potential renewable energy vector to replace the fossil fuels for its cost-effective, sustainable and clean properties.[1-4] Searching for efficient hydrogen storage materials remains one of the most critical challenges toward the H_2 energy based economy.[5-8] Recently, intensive interests have been focused on liquid storage materials, such as borane and especially formic acid, because of the high volumetric and weight energy density, and particularly the feasible handling and refuel, which can fit well with the current transportations.[9-16] Formic acid (FA, HCOOH), has attracted tremendous research interests due to its excellent stability, non-toxicity and possible regenerability by hydrogenation of carbon dioxide.[17-22] The decomposition of formic acid follows two principal pathways,[23-27] in which one process produces hydrogen (H_2) and carbon dioxide (CO_2) *via* the dehydrogenation reaction and the other produces water (H_2O) and carbon monoxide (CO) under dehydration reaction.

$$HCOOH\ (l) = CO_2\ (g) + H_2\ (g) \quad \Delta G = -35.0\ kJ\ mol^{-1} \quad (1)$$

$$HCOOH\ (l) = CO\ (g) + H_2O\ (g) \quad \Delta G = -14.9\ kJ\ mol^{-1} \quad (2)$$

The former reaction (equation (1)) is the desired one while the latter (equation (2)) is the undesired side reaction. Specifically, CO is a fatal poison to the most of the employed catalysts.[28]

It is reported that FA can be selectively dehydrogenated by homogeneous catalysts,[14, 29] which exhibits a superior catalytic effect at near ambient temperature.[30] However, homogeneous catalysts have difficulties in controlling, separating and recycling. Besides, they need the organic solvents/ligands/additives in the reaction systems.[31-34] These drawbacks prevent them from scaling-up for practical applications. Therefore, heterogeneous catalysts have attracted a great of interests for the selective decomposition of FA and much progress has been made recently.[11, 35] Nevertheless, for practical applications of heterogeneous catalysts on the dehydrogenation of FA, several issues should be carefully addressed. First, the catalysts should exhibit the sole selectivity for the dehydrogenation reaction. When polymer electrolyte membrane (PEM) fuel cells are used as the energy sources in the transportation, ultrapure hydrogen gas is required. Specifically, the gas stream has to be free from CO gas (< 10 ppm), or the catalytic performance of the fuel cells will be degraded significantly.[36] Improved catalytic effects have been achieved for the monodispersed nanoparticles, yet, traces of the CO (~ 20 ppm) are still detected during dehydrogenation.[37] Second, the heterogeneous catalysts should present the highly efficient catalytic effects. The heating system on board is complicated, thereby will intrinsically reduce the hydrogen capacities of the whole system dramatically. Besides, the undesired dehydration reaction for FA seems unavoidable at the

relatively higher catalysis temperature.[11] Third, most of the reported heterogeneous catalysts up to now consist of noble metals, including Pd, Au, and Pt, which greatly hinders the large-scale practical applications because of the high costs and low reserves in the earth's crust.[23, 38-42] Therefore, the architecture and the composition of the catalysts should be carefully designed and fabricated to reduce the consumption of the noble metals and meanwhile get a superior catalytic effect on the decomposition of FA at ambient temperature.

Strategies to overcome the above issues can be summarized into two main categories. The first strategy is to substitute the noble metals with relatively cheap metals and therefore fabricate and construct some alloy nanoparticles, such as AgPd, CuPd and CoAuPd.[37-39, 43, 44] Among these alloys, the AgPd has been proved to be the most effective one because of the inducing effect of Ag on the electron structure of the Pd.[11, 45] Another strategy is to reduce the particle size of the noble metals and get a well distribution of noble metal nanoparticles, thereby enhance the catalytic effects by increasing the ratio of the surface atoms in the total nanostructures.[23, 46]

Herein, we introduce a promising strategy to address these intricate issues by synthesizing a novel catalyst with hierarchical architecture and hollow structure arched on the ideal two-dimensional (2D) conducting structure of graphene. The AgPd hollow spheres (AgPd-Hs) with a diameter of about 18 nm and the wall thickness of about 5 nm arched on graphene (AgPd-Hs/G) were synthesized by one-pot co-reduction of GO and the metal precursors of Ag and Pd. To our knowledge, the synthesis of bimetallic core-shell and hollow structures generally needs templates or seeds and goes through at least two steps.[47-50] There are no related reports on the one-pot synthesis of hollow-sphere shaped AgPd supported on graphene. The previous galvanic exchange reactions generally based on silver nanoparticles as template to form porous or hollow nanoparticles.[49, 51, 52] In this work, AgPd-Hs can be formed without any seeds or templates. The hollow structure of AgPd nanoparticles (NPs) uniformly arched on the 2D graphene with ultrathin shells ensures that most of the atoms are located on the surface of the nanoparticles. Therefore catalytic sites are multiplied compared with the solid nanoparticles. The as-synthesized AgPd-Hs/G catalyst exhibits improved catalytic performance with an initial TOF value of as high as 333 mol H_2 mol^{-1} catalyst h^{-1}, a low activation energy value of 28 kJ mol^{-1} and without any CO generation toward the dehydrogenation of FA at room temperature.

Experimental Section

Materials

Graphite powder (99.85%, CP grade), sulfuric acid (H_2SO_4, AR grade), phosphoric acid (H_3PO_4, AR grade), potassium permanganate ($KMnO_4$, ≥ 99.5%), palladium (II) dihydrate ($Pd(NO_3)_2{\cdot}2H_2O$, ≥ 39.5% w/w (cont. Pd), nickel(II) nitrate hexahydrate ($Ni(NO_3)_2 \cdot 6H_2O$, ≥ 98%), cobalt(II) nitrate hexahydrate ($Co(NO_3)_2 \cdot 6H_2O$, ≥ 98.5%) and L-Ascorbic acid ($C_6H_8O_6$, ≥ 99.7%) were purchased from Sinopharm Chemical Reagent Co., Ltd. Pd/C (5% w/w (cont. Pd)), formic acid (CH_2O_2, 99%) and sodium formate ($CHNaO_2$, 99.5%) were obtained from Aladdin Reagent. Activated charcoal (C) and sodium borohydride ($NaBH_4$, ≥ 98%) were purchased from Acros Reagent. Silver nitrate ($AgNO_3$, ≥ 99.8%), trisodium citrate dihydrate ($C_6H_5Na_3O_7{\cdot}2H_2O$, ≥ 99.0%) and L-Ascorbic acid ($C_6H_8O_6$, ≥ 99.7%) were obtained from Shanghai Chemical Reagent. All agents were used as received without further purification.

Characterization

An X'Pert Pro X-ray diffractometer (PANalytical, the Netherlands) with Cu Kα radiation at 40 kV and 40 mA was applied to obtain the structural analysis of the sample. X-ray photoelectron spectroscopy (XPS) was carried on a VG ESCALAB MARK II system with Mg Kα radiation (1253.6 eV) at a base pressure of 1×10^{-8} torr. The spectra were recorded with the pass energy of 50 eV after Ar^+ sputtering of the surface for 15min. All binding energy values were referenced to the C_{1s} peak of contaminant carbon at 284.6 eV. The microstructures of doped materials were analyzed with a scanning electron microscope (SEM, Hitachi SU-70). Furthermore, transmission electron microscopy (TEM) images, high-resolution transmission electron microscopy (HRTEM) images, high-angle annular dark-field scanning transmission electron microscopy (HAADF-STEM) images, element analysis mapping and energy dispersive x-ray spectroscopy (EDX) carried out on a FEI Tecnai F20 (HR) microscopy operated at 200 kV were performed to observe the microstructure of the sample. Fourier transform infrared (FTIR) spectra were obtained with a Bruker Tensor 27 unit in transmission mode. The testing samples were prepared by cold-pressing a mixture of sample powder and potassium bromide (KBr) with a mass ratio of 1:300 to form a pellet. Each spectrum was plotted from 32 scans averaged with a solution of 4 cm^{-1}. The inductively coupled plasma-mass spectrometry (ICP-MS) was carried on a XSENIES (Thermo Electron Corporation, USA). Detailed analyses for CO_2 and CO were performed on SP-6890 with thermal conductivity detector (TCD) and flame ionization detector (FID)-Methanator.

Synthesis of graphene oxide (GO)

GO were obtained from graphite powder via an improved method by Daniela C. Marcan, et al.[53] Briefly, a 1:9 mixture of concentrated H_3PO_4/H_2SO_4 (40:360 mL) was added into 3 g of graphite powder. 18 g of potassium chlorate ($KMnO_4$) was added slowly to avoid sudden increase in temperature. Then, the solution was cooled to room temperature followed by kept at 50 ^oC and stirred for 12 h. Poured it out to a 500 mL beaker and added the ice (~ 400 mL) with enough 30% H_2O_2 until the color of the solution became from brown to bright yellow. After this progress, the resulting suspension was washed with water and the mixture was centrifuged. This water washing procedure was repeated several times and vacuum freeze-drying overnight, obtaining the expected product.

Synthesis of AgPd-Hs/G catalyst

Detailedly, 0.02 g GO was ultrasonically dispersed in 30 mL water and added to 0.275 g $C_6H_5Na_3O_7{\cdot}2H_2O$. The solution was

heated to boil. Under a gentle nitrogen flow, 5.0 mL of aqueous solution containing 0.0255 g (0.15 mmol) $AgNO_3$, 0.0269 g $Pd(NO_3)_2{\cdot}2H_2O$ (0.1 mmol) was added into the above suspension with magnetic stirring. After that, 2.0 mL of aqueous solution containing 0.176 g (1 mmol) L-AA was added following stirring for 2 h during which the brown solution gradually turned to black. After the reaction solution was cooled down to room temperature, the NPs were separated by adding water and centrifugation. To remove the impurities and precursor residues thoroughly, the product was redispersed in water and centrifugation for several times. Finally, the product was vacuum-dried overnight at 50 °C for further performance test. For comparison, Pd/G and AgPd/C were also prepared by the same method.

Hydrogen generation from FA/SF aqueous solution

Typically, the as-prepared AgPd-Hs/G catalyst and 10 mL water were kept in a two-necked round-bottom flask and preheated to the desired temperature. One neck was connected to a gas burette, and the other was connected to a pressure-equalization funnel to introduce FA/SF (2.5 M/2.5 M, 2 mL) aqueous solution. The catalytic reaction was begun once the mixture solution was added into the flask with magnetic stirring (400 r/min). The evolution of gas was monitored using the burette. The catalytic activities of other catalysts for FA decomposition were also applied as the above method.

Results and discussion

Figure 1 schematically shows the synthesis strategy for the AgPd-Hs/G nanocatalyst by a facile one-step hydrothermal reduction approach. Detailed procedures are shown in Experimental section in Supplementary Information. Firstly, the GO was dispersed in the sodium citrate aqueous solution. Then, at the temperature of 100 °C, the mixed precursor solution containing Ag^+ and Pd^{2+} was poured into the previous solution under inert atmosphere with magnetic stirring. After that, the aqueous solution of L-AA was added following stirring for 2 h during which the brown solution gradually turned to black. After the solution cooled down to room temperature, the AgPd-Hs/G was separated by adding water and centrifugation several times. Compared with other synthesis methods,[11, 49, 54] the present fabrication strategy was efficient and green by using L-AA as the reductant and trisodium citrate dihydrate as the stabilizer, without employing any seed, surfactant, organic solvent, template, stabilizing agent, or complicated apparatus.

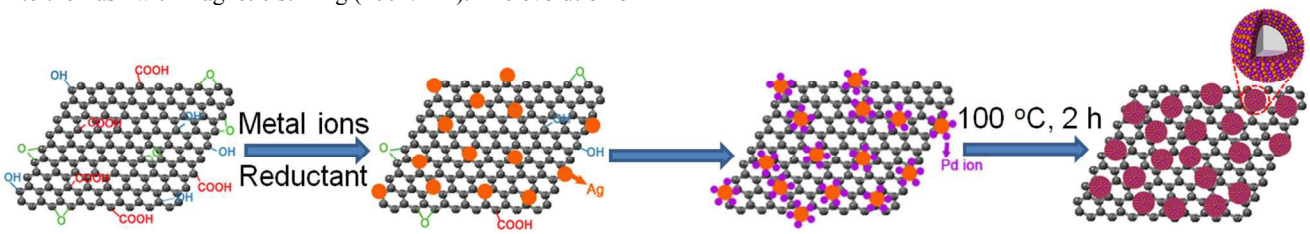

Fig. 1 Schematic illustration for preparation of AgPd-Hs/G. The preparation involves the galvanic reaction between the Pd ions and Ag nanoparticles.

X-ray diffraction (XRD) analysis was performed for the synthesized catalysts, as shown in Figure 2. Only Pd diffraction peaks can be detected for the Pd/G, indicating that the graphene is in the disordered state. Similar diffraction profiles were observed for the AgPd-Hs/G and AgPd/C. The XRD patterns of AgPd hybrids in both AgPd-Hs/G and AgPd/C catalysts show a series of diffraction peaks that located between the standard diffraction patterns of pure Pd (JCPDS: 68-2867) and Ag (JCPDS: 68-2871) with a face-centered cubic structure, which is due to the difference of the d-spacings between the alloys and the Pd- and Ag- species. Significantly broadened diffraction peaks of AgPd-Hs/G and AgPd/C indicate that the *in situ* formed AgPd NPs are in nanocrystallinity. The average crystal size for the AgPd NPs in the AgPd-Hs/G composite was calculated from the largest diffraction peaks by using Scherrer's equation, and the estimated average crystal size was about 5.1 nm. We also used Bragg equation to calculate the lattice spacing for the (111) planes of AgPd-Hs/G, the result was 0.232 nm. While the average crystal size for the AgPd NPs of AgPd/C was calculated to be about 5.5 nm and the lattice spacing of the (111) planes was 0.232 nm.

The detailed morphologies for the synthesized catalysts were studied by using scanning electron microscopy (SEM), transmission electron microscopy (TEM), high-resolution transmission electron microscopy (HRTEM), energy dispersive X-ray (EDX) and selected area electron diffraction patterns (SAED). The representative SEM image of the AgPd-Hs/G catalyst shows that ultra small white dots with size less than 20 nm are homogeneously dispersed on the support (Figure S1). These white dots can be ascribed to be the as-synthesized AgPd NPs. Combining the above result with the corresponding energy dispersive X-ray (EDX) spectrum, it can be concluded that the AgPd NPs are successfully formed and uniformly arched on the graphene.

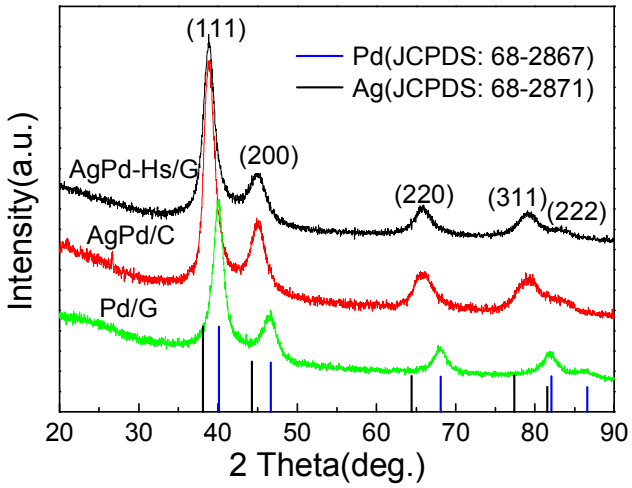

Fig. 2 XRD patterns for the as-synthesized AgPd-Hs/G, AgPd/C and Pd/G.

XPS spectra were performed to further confirm the existence of Ag and Pd metallic state. From Figure 3, it can be seen that the XPS spectra of Pd can be deconvoluted into four peaks, indicating that Pd is present in the hollow sphere-shaped nanocrystals as both metallic Pd and PdO. The XPS signals from the oxidation states of palladium may be from the partial adsorption of excessive Pd^{2+} precursor on the Ag nanoparticles. On the other hand, the observation of the Ag $3d_{3/2}$ and Ag $3d_{5/2}$ peaks indicates that Ag is present in the metallic state. The peaks of Pd^0 and Ag^0 demonstrate the co-existence of both metals.

Figure 4a and b show the typical TEM images for the as-prepared AgPd-Hs/G. It is clear that the NPs are well-dispersed on graphene with an average particle size of about 18 nm, while the pore size is about 8 nm and the shell thickness is about 5 nm. In the process of preparing AgPd-Hs/G, metal NPs act as nanoscaled spacers and deposit on the surface, which increases the interlayer spacing between graphene sheets and successfully prevents the stacks of the graphene to graphite.[55] The ultra-high specific surface area with high conductivity of graphene gives the positive effects on the supported catalysts.[9, 16, 56, 57] Severe aggregation also appears without using GO but C as the support (Figure S2a). A typical TEM image with the corresponding histograms of particle size distribution is shown in Figure S2b. The size distribution is derived from the TEM image by counting 100 particles. From the plot, the mean size of particles is found to be about 18 nm. We further used HRTEM, EDX, line-scan EDX spectrum and high-angle annular dark-field scanning transmission electron microscopy (HAADF-STEM) to characterize the morphology, structure, and composition of the AgPd-Hs nanocrystals. Figure 4c shows a typical HRTEM image of an individual AgPd hollow sphere. As can be seen, the lattice spacing is measured to be 0.232 nm, which is in good accordance with the calculated result of XRD using Bragg equation. The d-spacing value is between the value of the (111) planes of face-centered cubic (fcc) Ag (0.236 nm) and Pd (0.224 nm). The HAADF-STEM microscopy image in Figure 4d clearly shows the hollow-spherical structure of AgPd nanoparticle, from which the particle shows a clear contrast between the interior and exterior. The corresponding EDX spectrum further demonstrates the existence of Ag, Pd and C elements in the AgPd-Hs/G sample (Figure 4e and Figure S1). To further investigate the distribution of the Ag and Pd in the AgPd-Hs, cross-sectional compositional line profile and elemental mapping were performed. Figure 4g shows line analysis data along the red line depicted in Figure 4f. It is obvious that the Ag has two peaks and the Pd also has two peaks. These two peaks for Ag and Pd are perfectly overlapped and concentrated at the shell of the nanosphere. Figure 4i and j show the EDX mapping images of Pd and Ag elements, respectively. From EDX mapping images of the single particle, distinct contrast between the shell and the interior for the nanoparticle is observed which confirms its hollow structure and AgPd alloy shell composition. Electron microscopy investigations suggest that the alloy structure is formed in the wall of AgPd-Hs.

Considering that the standard reduction potential of Ag^+/Ag pair is typically more negative than that of Pd^{2+}/Pd when they are in the same environment, it seems impossible and contradictory to fabricate hollow metal alloy materials in one-step. That is, Palladium (II) should be reduced before silver (I) as expected from the reduction potentials, resulting that the galvanic reaction between silver (0) and Palladium (II) would not occur in the system.

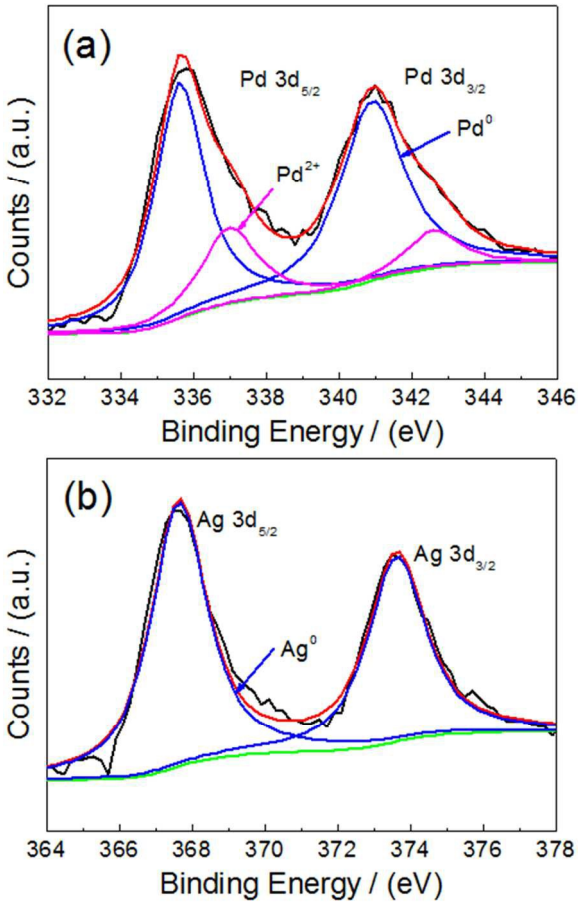

Fig. 3 XPS spectra of Pd 3d (a) and Ag 3d (b) of AgPd-Hs/G.

As we know from the above result, GO plays an important role on the good dispersion of metal NPs. It is speculated that the GO is related to the formation of AgPd-Hs NPs on its surface. To better understand the formation mechanism of hollow spheres, we investigated the activated carbon as supporting matrix instead of GO during synthesis. Severe aggregation appeared and few hollow-spheres were formed (Figure S2a) which strongly proved our assumption. Therefore, the oxygen-containing groups that only on the GO play an vital role in the formation of AgPd-Hs NPs which accelerate the reduction of Ag^+ to Ag atoms and the galvanic replacement occurs afterwards. Some of the oxidized Ag^+ were reduced by the reductant during the diffusion process resulting the fabrication of the alloy shell. Huang et al.[58] also reported that the presence of acetylacetonate ions in the system could alter the reduction kinetic of Pd and Pt metal cations and therefore be critical to the one-pot formation of PdPt hollow structure. Besides, many other conditions such as special ions like Br^- and SO_4^{2-}, reduction agent, pH and temperature are also crucial for the transformation of the reduction kinetics of metal ions.[58-60]

To further ascertain the formation mechanism of AgPd-Hs/G,

we did more experiments to verify if hollow structure nanoparticles could be synthesized under other conditions. As can be seen, without the addition of trisodium citrate dihydrate (Figure S3a and S3c) or using carbon instead of graphene (Figure S3b and S3d) as support, no uniform hollow sphere-shaped nanoparticles were synthesized successfully. It can be concluded that hollow structure nanoparticles can only be synthesized under some certain condition and the formation depends on many factors like support or other additions.

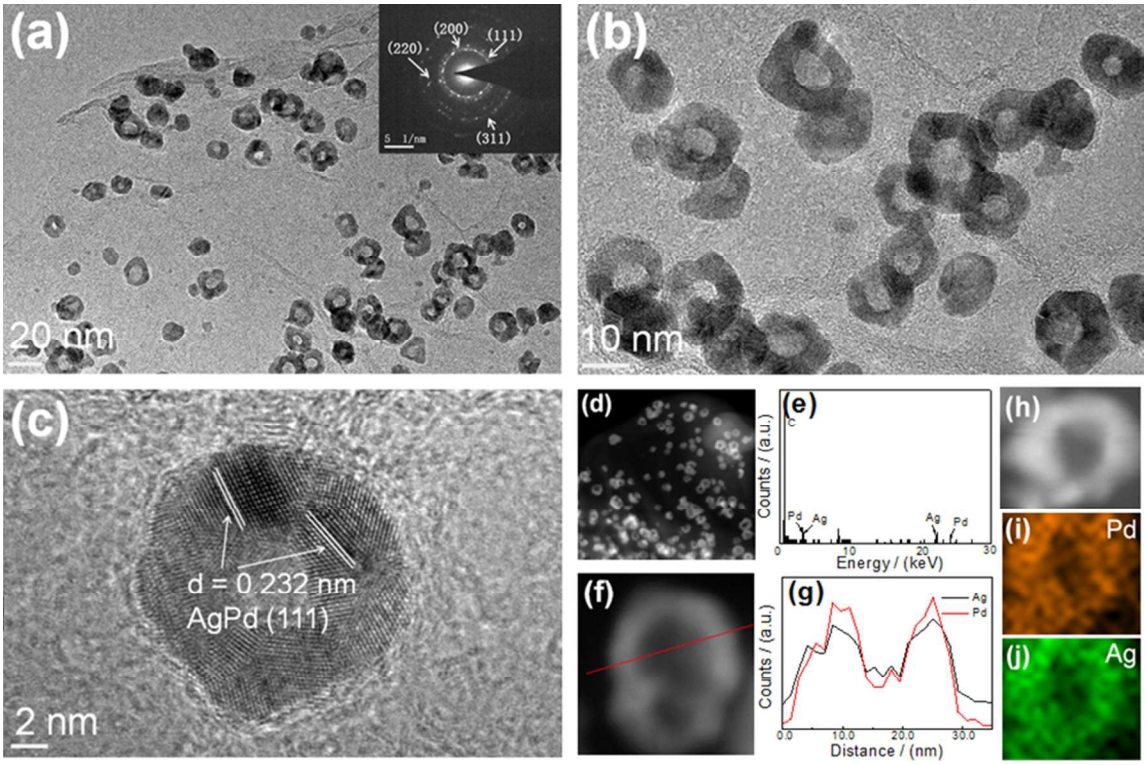

Fig. 4 TEM (a), enlarged TEM (b), HRTEM (c) and HAADF-STEM (d) images of AgPd-Hs/G, the inset of (a) shows the corresponding SAED pattern. EDS analysis (e) and Cross-sectional compositional line profile (g) along the red line shown in (f) of a AgPd hollow sphere, and HAADF-STEM-EDS mapping images (h, i, j) of a AgPd hollow sphere.

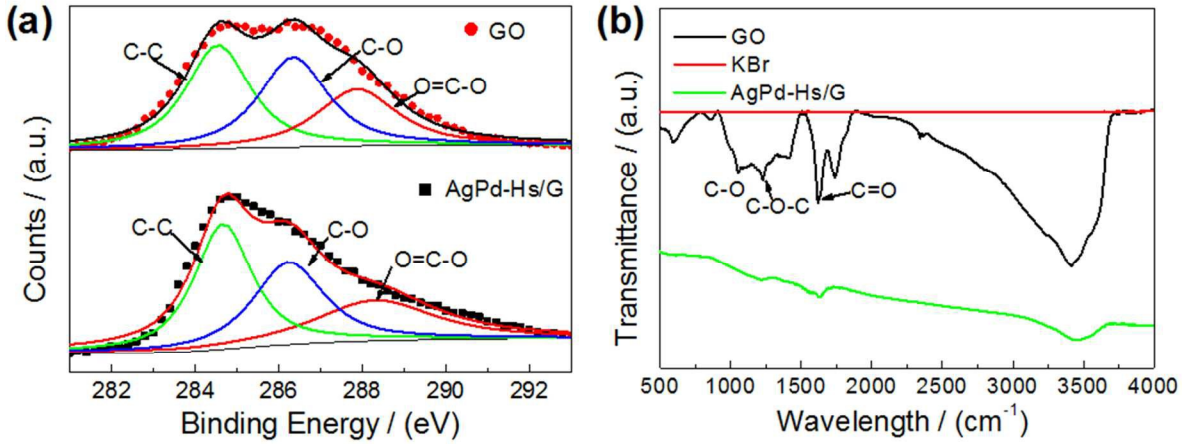

Fig. 5 XPS spectra of C_{1s} (a) on GO (red line) and AgPd-Hs/G (black line) and FT-IR (b) spectra of GO, KBr and AgPd-Hs/G.

During the reduction process of Ag and Pd precursors, GO was reduced by L-AA. XPS analysis was conducted on the AgPd-Hs/G sample to investigate the local atomic environment of the surface for C_{1s} species in the composite. As shown in Figure 5a, C-C bonds (284.6 eV) become predominant while the additional peak of C-O (286.6 eV) is significantly reduced compared with the binding energy of C_{1s} on the GO surface. The presence of oxygen-functional groups like –COOH, -OH, C=O on the GO can not only act as the nucleation sites and facilitate seeding and growth of hollow nanoparticles but also improve the accessibility and wettability with aqueous solution and improve the performance of the catalyst.[61, 62] In addition, Sharma et al.[63] found that the residual oxygen functional groups played a major role on the removal of carbonaceous species from the adjacent sites which was the main reason for the CO-tolerance which was of significance in the energy-related applications. The reduction of

the oxygen-containing groups in GO was also confirmed by Fourier Transform Infrared (FT-IR) spectroscopy. As shown in Figure 5b, after the reduction, the intensities of the peaks corresponding to the oxygen functionalities, such as C-O, C-O-C and C=O stretching vibration peaks decrease dramatically, and some of them disappear entirely. These observations confirm that most oxygen functionalities of the GO are removed. Raman spectrum of the AgPd-Hs/G catalyst was performed as depicted in Figure S4. Raman spectrum is widely regarded as a typical detection used to determine the ordered and disordered crystalline structure of graphene. For graphene oxide, the two peaks at 1350 and 1580 cm^{-1}can be assigned to the D-band (the symmetry A_{1g} mode) and G-band (the E_{2g} mode of sp^2 carbon atoms), respectively. With the reduction, the ratio of D- and G-band in the GO increase revealing the change of the electronic conjugation state.[64] I_D/I_G ratio is proportional inversely to the reciprocal of the crystallite size of carbon-based materials. As seen in the Figure S4, G peak has an asymmetric feature composed of two partly overlapped peaks that is G and D′ peaks. In fact, the D′ peak at 1620 cm^{-1} is a defect peak related to intra-valley scattering.[65] Compared to that of the original GO, AgPd-Hs/G exhibits a significant increase of D/G intensity ratio, implying the ordered crystal structure of reduced graphene and the decreased size of the in-plane sp^2 domains. This agrees well with the Raman spectra of the GO reduced by reductants that were reported by Zhang et al.[66] and Stankovich et al.[67] The result indicates that the reduction does take place.

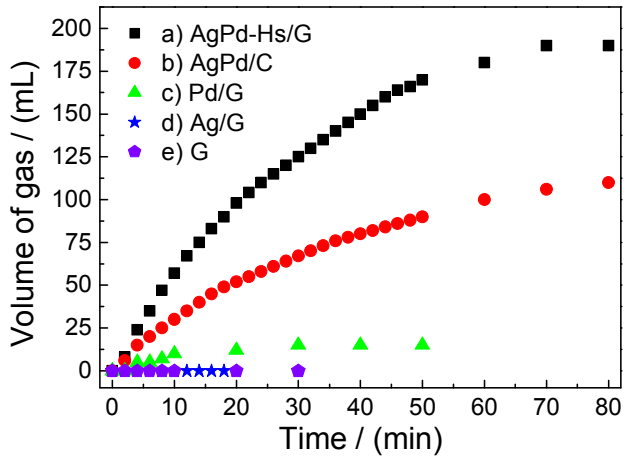

Fig. 6 Gas generation by the decomposition of FA/SF (2.5 M/2.5 M, 2 mL) versus time in the presence of AgPd-Hs/G (a), AgPd/C (b), Pd/G (c), Ag/G (d), G (e) at 25 °C under ambient atmosphere.

The as-synthesized AgPd-Hs/G, AgPd/C, Pd/G, Ag/G together with the as-synthesized graphene (G) were evaluated as catalysts for H_2 generation from FA decomposition at 25 °C under ambient atmosphere. The results are presented in Figure 6. Obviously, AgPd-Hs/G exhibits a much better activity than AgPd/C, Pd/G, Ag/G and G catalysts synthesized by the same method. That is, AgPd-Hs/G exhibits much higher gas volume toward formic acid, which is almost two times than that of AgPd/C. The initial TOF of AgPd-Hs/G is measured at 25 °C in the first 10 minutes of gas generation. From Figure 6, it is also obvious that Pd atoms are the crucial active sites in all the prepared catalysts. Namely, without Pd participation, Ag/G and G show no activities at all. On the contrary, with Pd addition, the activities of AgPd-Hs/G, AgPd/C and Pd/G have been enhanced obviously. AgPd-Hs/G exhibits a better performance than Pd/G because of the synergistic effect between Pd and Ag. Palladium (5.1eV) has the larger work function than that of silver (4.7eV), the electron can transfer from the Ag to the Pd. The interaction between the two metals promotes the catalytic activity of the catalyst.

To further investigate if graphene has a dramatic effect on the AgPd-Hs/G hybrids, we substituted graphene with activated carbon and synthesized AgPd/C. It can be seen that the catalytic activity of AgPd-Hs/G is almost two times than that of AgPd/C, suggesting that the graphene plays a key role on the AgPd-Hs/G hybrids and the synergistic coupling between AgPd-Hs and graphene. In a word, graphene was used as the support and the suspended bonds on the oxide graphene play an important role for the uniform distribution of the AgPd nanoparticles during the synthesis. On the other hand, graphene can also facilitate the formation of the catalyst's unique hollow-spherical shape structure.

The composition of the AgPd-Hs was analyzed by inductively coupled plasma-mass spectrometry (ICP-MS) (Table S1). The mass ratio between Ag and Pd is 1:1.46. The molar ratio of Ag and Pd precursors can be adjusted for further investigation. The initial TOF is calculated to be 333 mol H_2 mol^{-1} catalyst h^{-1} at 25 °C under ambient atmosphere, which is larger than that of the most active catalysts ever reported (Table S2).

We also tested the catalysts reduced by different reducing agents of L-AA and $NaBH_4$. As shown in Figure S5, it is clear that the catalytic activity of the catalyst reduced by L-AA (AgPd-Hs/G) is better than that of reduced by $NaBH_4$. The formation of AgPd/G reduced by $NaBH_4$ has been confirmed by the XRD patterns in supporting information Figure S6. The XRD patterns of AgPd hybrids in catalyst show a series of diffraction peaks that located between the standard diffraction patterns of pure Pd (JCPDS: 68-2867) and Ag (JCPDS: 68-2871) with a face-centered cubic structure. The XPS spectrum (Figure S7) indicates that Pd^0 and Ag^0 peaks are present, which demonstrates the co-existence of both Ag and Pd metals. The typical TEM images in Figure S8a and S8b show the as-prepared AgPd anchored on graphene (denoted as AgPd/G) reduced by $NaBH_4$. It is clear that the NPs are dispersed on graphene with an average particle size of about 5nm. Some particles agglomerate severely. Figure S8c shows a typical HRTEM image of an individual AgPd nanoparticle. As can be seen, the lattice spacing is measured to be 0.228 nm, which is in good accordance with the calculated result of XRD using Bragg equation and also between the value of the (111) planes of face-centered cubic (fcc) Ag (0.236 nm) and Pd (0.224 nm). Figure S8e and S8f show the EDX mapping images of Ag and Pd elements, respectively. From EDX mapping images of the single particle, Ag and Pd are perfectly overlapped which confirms the AgPd alloy composition.

Although the particle size of AgPd/G is smaller than that of AgPd-Hs/G (the average particle size of about 18 nm), the performance of AgPd/G is better than the latter which due to the different structure between the two catalysts that AgPd/G is the alloy structure while AgPd-Hs/G is the hollow-spherical shape. The hollow structure ensures most of the atoms are located on the

surface or sub-surface of the spheres, resulting in more catalytic sites.

To obtain the activation energy (E_a) of the dehydrogenation of FA catalyzed by AgPd-Hs/G, we carried out the catalytic reactions at different temperatures in the range of 40 to 70 °C (Figure 7a). The gas almost releases completely in 20 min at 70 °C. The values of rate constant k at different temperatures are calculated from the slope of the linear part of each plot from Figure 7a. Figure 7b is the Arrhenius plot of ln k vs $1/T$, from which the apparent E_a is determined to be approximately 28 kJ mol^{-1}. This value is among the lowest values ever reported for the heterogeneous catalysts (Table S2). For example, Ping et al.[45] employed a facile co-reduction route to prepare AgPd alloy supported on graphene (AgPd/rGO). The TOF of the catalyst was calculated to be only 105.2 mol H_2 mol^{-1} catalyst mol^{-1} h^{-1} at 25 °C. Tedsree et al.[11] prepared Ag@Pd using a two-step method with PVP as the dispersing agent which showed a catalytic activity with TOF of 252 mol H_2 mol^{-1} catalyst h^{-1} at 50 °C. After the catalytic performance test, the evolution of morphology of AgPd-Hs/G was investigated by TEM to further understand their structural stability. As shown in Figure S1c, it is obvious that AgPd-Hs kept their original structure.

To investigate the role of water, we substituted the water with alcohol. That is, the as-prepared catalyst and 10 mL alcohol were kept in a two-necked round-bottom flask and preheated to the desired temperature with other conditions uniformly. From the result (Figure S9), it is obvious that the catalyst shows better catalytic activity using water as the solvent than that of alcohol. The results can be explained by that the proton in aqueous solution is a necessary condition for the decomposition of FA. The result is consistent with the principle of FA decomposition proposed by Hu et al.[68] and Gao et al.[69] In addition, Akiya et al.[70] suggested that the presence of water reduced the activation barrier for the decomposition and had a strong effect on the relative stability of the transition state which played an important role in determining the decomposition pathway. We also tested other alloy catalysts supported on graphene, as shown in Figure S6, it can be concluded that AgPd-Hs/G has the best catalytic activity among any other alloy catalysts tested in this work.

Catalyst poisoning induced by CO is an inherent damage for a variety of applications no matter CO appears as a reactant, a reaction byproduct or an impurity in the reactant. For many practical applications, the absence of CO is a vital factor. Therefore, we measured the content of CO for AgPd-Hs/G in the catalytic decomposition of FA using gas chromatograph (GC). Our result shows that the AgPd-Hs/G catalyst releases no CO (Figure 8), which means that the present AgPd-Hs/G catalyst has a high H_2 selectivity for FA decomposition. That is, for AgPd-Hs/G, CO can be efficiently inhibited and the released gas can be directly used in fuel cells. Because of the large volume ratio between CO and CO_2, the CO_2 peak can't appear completely, and vice versa.

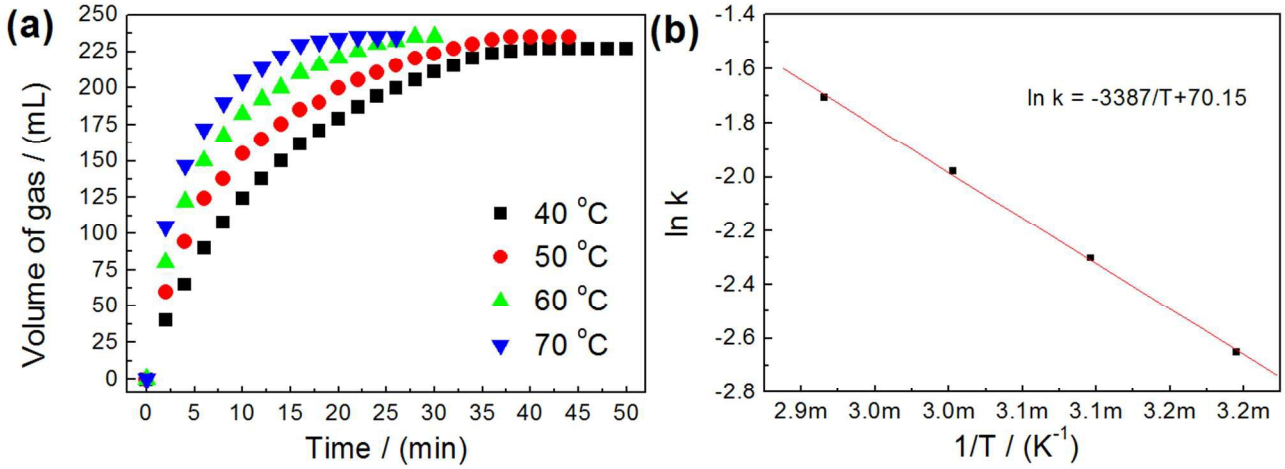

Fig. 7 Time course plots for hydrogen generation by the decomposition of FA by AgPd-Hs/G at 40, 50, 60, 70 °C (a) and Arrhenius plot of ln k vs $1/T$ (b).

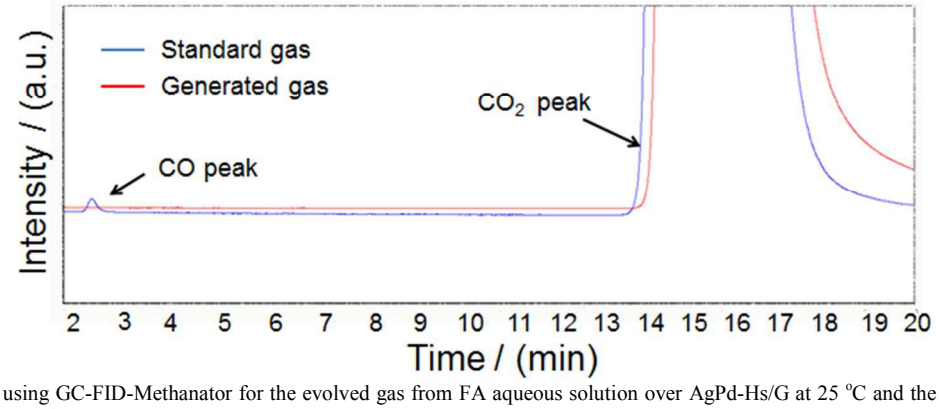

Fig. 8 GC spectrum using GC-FID-Methanator for the evolved gas from FA aqueous solution over AgPd-Hs/G at 25 °C and the standard gas containing CO and CO_2 of volume ratio 1:4500.

The cycling performance of the AgPd-Hs/G catalyst was assessed and the representative cycling curves are shown in Figure S10. As seen from this figure, there was a slight deactivation when second trial of the supported catalyst under identical mixture was conducted. It is not yet known the reason of deactivation. The CO poisoning from formic acid dehydration was ruled out since there was no any CO detected in the gas mixture. TEM images from Figure S2 also show that the morphology and structure of the catalyst maintain the same after the catalytic test. We also performed XPS to see if the metals were oxidized during the catalytic test. From XPS spectrum in Figure 3 and S11, we can know that there is no difference between the catalysts before and after the catalytic performance test demonstrating no oxidation of both Ag and Pd metals. It is speculated that there was small losses of supported catalyst or minor degree of nanoparticles detachment from the support during the test.

We cannot rule out some by-products or intermediates were trapped in the porous catalyst, leading to the slight deactivation. More detailed study is therefore required. Strategies including adding additives for desorption of strong adsorbent(s) and electrical pulses heating of the carbon sample for regeneration are possible if deactivation is unavoidable after a number of cycles.

As shown in the results presented above, the as-synthesized AgPd-Hs/G displays a superior catalytic effect on the dehydrogenation of FA without any generation of CO at temperature as low as 25 ^{o}C. After the catalytic performance test, the morphology, distribution and structure of the catalyst remain the same. Besides the morphology and distribution, there is no oxidation state for both Pd and Ag metals in the catalyst which clearly reveal the excellent stability of the prepared catalyst. These highly active properties for AgPd-Hs/G should be attributed to their distinct architecture, electronic structure and morphology that offer the following benefits. Firstly, it has been proved that Pd is the most effective monometallic nanoparticles for the dehydrogenation of FA.[11, 44] Yet, their catalytic activity and the selectivity are still very poor and not active enough for the dehydrogenation of FA at ambient temperature.[37, 44] The presence of Ag increased the activity of alloy nanoparticles due to the inductive effects. Secondly, the hollow structure with a very thin wall is of great interest in the application of catalysis, since only the atoms on the surface or the sub-surface can provide the reactive sites for catalysis. Large quantities of bulk atoms located within the interior of the nanoparticles are actually not involved in the catalysis reaction. Thirdly, well dispersion of the AgPd hollow spheres on the graphene ensures well transport of the different species and favorable electrical conductivity in the catalytic processes.

Conclusions

In summary, we have reported a simple wet-chemical method for the synthesis of AgPd hollow spheres arched on graphene with excellent catalytic activity and high H_2 selectivity for H_2 generation from aqueous solution of FA at room temperature. Compared with other catalyst systems, the present AgPd-Hs/G shows superior performance. The initial TOF reaches a high value of 333 mol H_2 mol^{-1} catalyst h^{-1} at 25 ^{o}C under ambient atmosphere. The activation energy of the catalyst is 28 kJ mol^{-1}, which is among the lowest values ever reported for the heterogeneous catalysts, indicating a reduced kinetic barrier. We also prove the importance of water in the catalytic system. The exceptionally high TOF value originates from the modified electronic structure of Pd in AgPd-Hs/G, the strong metal–support interaction between AgPd hollow spheres and the graphene support and also the ultrafine and good dispersion of the AgPd hollow spheres supported on graphene. The hollow architecture with thin outer shells dramatically increases the surface area of catalytic active sites. The present AgPd-Hs/G with efficient catalysis on the decomposition of formic acid without any CO generation at room temperature can pave the way for the practical liquid H_2 storage system and therefore promote the application of formic acid on fuel cell systems. It is anticipated that the present synthesis of the graphene supported AgPd hollow spheres can also be extended on the catalysis for other applications, such as full cells, Suzuki-Miyaura reactions *etc*.

Acknowledgements

The authors gratefully acknowledge the financial support for the research from the National Natural Science Foundation of China (Grants 21303161, 51471151, 51171173), the Program for Innovative Research Team in University of Ministry of Education of China (Grant IRT13037), and Zhejiang Provincial Science & Technology Program of China (Grant 2014C31134).

Notes and references

State Key Laboratory of Silicon Materials, Key Laboratory of Advanced Materials and Application for Batteries of Zhejiang Province, Department of Materials Science and Engineering, Zhejiang University, Hangzhou 310027, PR China. Fax: +86 571 87951152 Tel: +86 571 87951152; E-mail: lxchen@zju.edu.cn

† Electronic Supplementary Information (ESI) available: [SEM-EDS, TEM and the corresponding histograms of particles size distribution, Raman spectra, Gas generation curves, ICP-MS analysis, Comparision of activities of different catalysts, Calculation method for TOF]. See DOI: 10.1039/b000000x/

1 Z. W. Zhang, W. T. Zheng and Q. Jiang, *Int J Hydrogen Energ*, 2012, **37**, 5090-5099.
2 J. M. Yan, Z. L. Wang, H. L. Wang and Q. Jiang, *J Mater Chem*, 2012, **22**, 10990-10993.
3 L. Schlapbach and A. Zuttel, *Nature*, 2001, **414**, 353-358.
4 T. C. Johnson, D. J. Morris and M. Wills, *Chem Soc Rev*, 2010, **39**, 81-88.
5 J. Yang, A. Sudik, C. Wolverton and D. J. Siegel, *Chem Soc Rev*, 2010, **39**, 656-675.
6 J. A. Turner, *Science*, 2004, **305**, 972-974.
7 M. Felderhoff, C. Weidenthaler, R. von Helmolt and U. Eberle, *Phys Chem Chem Phys*, 2007, **9**, 2643-2653.
8 S. Enthaler, *ChemSusChem*, 2008, **1**, 801-804.
9 L. Yang, W. Luo and G. Cheng, *ACS applied materials & interfaces*, 2013, **5**, 8231-8240.
10 K. Aranishi, H. L. Jiang, T. Akita, M. Haruta and Q. Xu, *Nano Res*, 2011, **4**, 1233-1241.
11 K. Tedsree, T. Li, S. Jones, C. W. A. Chan, K. M. K. Yu, P. A. J. Bagot, E. A. Marquis, G. D. W. Smith and S. C. E. Tsang, *Nat Nanotechnol*, 2011, **6**, 302-307.

12 C. H. Liu, X. Q. Chen, Y. F. Hu, T. K. Sham, Q. J. Sun, J. B. Chang, X. Gao, X. H. Sun and S. D. Wang, *ACS applied materials & interfaces*, 2013, **5**, 5072-5079.

13 H. L. Jiang, S. K. Singh, J. M. Yan, X. B. Zhang and Q. Xu, *ChemSusChem*, 2010, **3**, 541-549.

14 M. Yadav and Q. Xu, *Energ Environ Sci*, 2012, **5**, 9698-9725.

15 M. Chandra and Q. Xu, *J Power Sources*, 2006, **156**, 190-194.

16 J. Wang, Y. L. Qin, X. Liu and X. B. Zhang, *J Mater Chem*, 2012, **22**, 12468-12470.

17 M. G. Mura, L. De Luca, G. Giacomelli and A. Porcheddu, *Adv Synth Catal*, 2012, **354**, 3180-3186.

18 S. Enthaler, J. von Langermann and T. Schmidt, *Energ Environ Sci*, 2010, **3**, 1207-1217.

19 R. S. Haszeldine, *Science*, 2009, **325**, 1647-1652.

20 J. F. Hull, Y. Himeda, W. H. Wang, B. Hashiguchi, R. Periana, D. J. Szalda, J. T. Muckerman and E. Fujita, *Nat Chem*, 2012, **4**, 383-388.

21 M. Grasemann and G. Laurenczy, *Energ Environ Sci*, 2012, **5**, 8171-8181.

22 Q. L. Zhu and Q. Xu, *Energ Environ Sci*, 2015, **8**, 478-512.

23 Z. L. Wang, J. M. Yan, H. L. Wang, Y. Ping and Q. Jiang, *Scientific reports*, 2012, **2**, 1-6.

24 Q. Y. Bi, X. L. Du, Y. M. Liu, Y. Cao, H. Y. He and K. N. Fan, *Journal of the American Chemical Society*, 2012, **134**, 8926-8933.

25 A. Boddien and H. Junge, *Nat Nanotechnol*, 2011, **6**, 265-266.

26 M. Czaun, A. Goeppert, R. May, R. Haiges, G. K. S. Prakash and G. A. Olah, *ChemSusChem*, 2011, **4**, 1241-1248.

27 B. Loges, A. Boddien, F. Gartner, H. Junge and M. Beller, *Top Catal*, 2010, **53**, 902-914.

28 S. Park, Y. Xie and M. J. Weaver, *Langmuir*, 2002, **18**, 5792-5798.

29 G. Mazzone, M. E. Alberto and E. Sicilia, *J Mol Model*, 2014, **20**. Doi:10.1007/s00894-014-2250-4.

30 A. Boddien, D. Mellmann, F. Gartner, R. Jackstell, H. Junge, P. J. Dyson, G. Laurenczy, R. Ludwig and M. Beller, *Science*, 2011, **333**, 1733-1736.

31 S. Fukuzumi, T. Kobayashi and T. Suenobu, *Journal of the American Chemical Society*, 2010, **132**, 1496-+.

32 A. Boddien, B. Loges, F. Gartner, C. Torborg, K. Fumino, H. Junge, R. Ludwig and M. Beller, *Journal of the American Chemical Society*, 2010, **132**, 8924-8934.

33 A. Boddien, F. Gartner, D. Mellmann, P. Sponholz, H. Junge, G. Laurenczy and M. Beller, *Chimia*, 2011, **65**, 214-218.

34 O. Metin, X. L. Sun and S. H. Sun, *Nanoscale*, 2013, **5**, 910-912.

35 X. C. Zhou, Y. J. Huang, C. P. Liu, J. H. Liao, T. H. Lu and W. Xing, *ChemSusChem*, 2010, **3**, 1379-1382.

36 T. E. Springer, T. Rockward, T. A. Zawodzinksi and S. Gottesfeld, *J Electrochem Soc*, 2001, **148**, I9-I9.

37 Y. J. Huang, X. C. Zhou, M. Yin, C. P. Liu and W. Xing, *Chem Mater*, 2010, **22**, 5122-5128.

38 S. Zhang, O. Metin, D. Su and S. H. Sun, *Angew Chem Int Edit*, 2013, **52**, 3681-3684.

39 Z. L. Wang, J. M. Yan, Y. Ping, H. L. Wang, W. T. Zheng and Q. Jiang, *Angew Chem Int Edit*, 2013, **52**, 4406-4409.

40 D. A. Bulushev, L. J. Jia, S. Beloshapkin and J. R. H. Ross, *Chem Commun*, 2012, **48**, 4184-4186.

41 D. A. Bulushev, L. J. Jia, S. Beloshapkin and J. Ross, *Abstr Pap Am Chem S*, 2012, **243**.

42 E. O. Kilic, A. S. Koparal and U. B. Ogutveren, *Fuel Process Technol*, 2009, **90**, 158-163.

43 Z. L. Wang, H. L. Wang, J. M. Yan, Y. Ping, S. I. O, S. J. Li and Q. Jiang, *Chem Commun*, 2014, **50**, 2732-2734.

44 X. C. Zhou, Y. J. Huang, W. Xing, C. P. Liu, J. H. Liao and T. H. Lu, *Chem Commun*, 2008, **DOI: Doi 10.1039/B803661f**, 3540-3542.

45 Y. Ping, J. M. Yan, Z. L. Wang, H. L. Wang and Q. Jiang, *Journal of Materials Chemistry A*, 2013, **1**, 12188-12191.

46 M. Ojeda and E. Iglesia, *Angew Chem Int Edit*, 2009, **48**, 4800-4803.

47 Y. Y. Jiang, Y. Z. Lu, D. X. Han, Q. X. Zhang and L. Niu, *Nanotechnology*, 2012, **23**, 105609.

48 Z. Y. Bai, L. Yang, L. Li, J. Lv, K. Wang and J. Zhang, *J Phys Chem C*, 2009, **113**, 10568-10573.

49 M. M. Liu, Y. Z. Lu and W. Chen, *Adv Funct Mater*, 2013, **23**, 1289-1296.

50 Y. Guo, Y. T. Xu, G. H. Gao, T. Wang, B. Zhao, X. Z. Fu, R. Sun and C. P. Wong, *Catal Commun*, 2015, **58**, 40-45.

51 J. Y. Chen, B. Wiley, J. McLellan, Y. J. Xiong, Z. Y. Li and Y. N. Xia, *Nano Lett*, 2005, **5**, 2058-2062.

52 J. Y. Chen, J. M. McLellan, A. Siekkinen, Y. J. Xiong, Z. Y. Li and Y. N. Xia, *Journal of the American Chemical Society*, 2006, **128**, 14776-14777.

53 D. C. Marcano, D. V. Kosynkin, J. M. Berlin, A. Sinitskii, Z. Z. Sun, A. Slesarev, L. B. Alemany, W. Lu and J. M. Tour, *Acs Nano*, 2010, **4**, 4806-4814.

54 M. Hattori, H. Einaga, T. Daio and M. Tsuji, *Journal of Materials Chemistry A*, 2015, **3**, 4453-4461.

55 R. Pasricha, S. Gupta and A. K. Srivastava, *Small*, 2009, **5**, 2253-2259.

56 S. J. Guo, S. J. Dong and E. K. Wang, *Acs Nano*, 2010, **4**, 547-555.

57 Y. She, Z. Lu, W. Fan, S. Jewell and M. K. H. Leung, *Journal of Materials Chemistry A*, 2014, **2**, 3894.

58 X. Q. Huang, H. H. Zhang, C. Y. Guo, Z. Y. Zhou and N. F. Zheng, *Angew Chem Int Edit*, 2009, **48**, 4808-4812.

59 K. J. Lee, Y. I. Lee, J. Lee, N. V. Myung and Y. H. Choa, *Curr Appl Phys*, 2012, **12**, S53-S58.

60 B. S. Choi, S. M. Kim, J. Gong, Y. W. Lee, S. W. Kang, H. S. Lee, J. Y. Park and S. W. Han, *Chem-Eur J*, 2014, **20**, 11669-11674.

61 M. Pumera, *Chem Soc Rev*, 2010, **39**, 4146-4157.

62 Y. L. Qin, J. W. Wang, Y. M. Wu and L. M. Wang, *Rsc Adv*, 2014, **4**, 30068-30073.

63 S. Sharma, A. Ganguly, P. Papakonstantinou, X. P. Miao, M. X. Li, J. L. Hutchison, M. Delichatsios and S. Ukleja, *J Phys Chem C*, 2010, **114**, 19459-19466.

64 F. Tuinstra and J. L. Koenig, *J Chem Phys*, 1970, **53**, 1126-&.

65 J. Xie, Y. X. Zheng, S. Y. Liu, W. T. Song, Y. G. Zhu, G. S. Cao, T. J. Zhu and X. B. Zhao, *Int J Electrochem Sc*, 2012, **7**, 1319-1331.

66 J. L. Zhang, H. J. Yang, G. X. Shen, P. Cheng, J. Y. Zhang and S. W. Guo, *Chem Commun*, 2010, **46**, 1112-1114.

67 S. Stankovich, D. A. Dikin, R. D. Piner, K. A. Kohlhaas, A. Kleinhammes, Y. Jia, Y. Wu, S. T. Nguyen and R.S. Ruoff, *Carbon*, 2007, **45**, 1558-1565.

68 C. Q. Hu, J. K. Pulleri, S. W. Ting and K. Y. Chan, *Int J Hydrogen Energ*, 2014, **39**, 381-390.

69 W. Gao, J. A. Keith, J. Anton and T. Jacob, *Dalton T*, 2010, **39**, 8450-8456.

70 N. Akiya and P. E. Savage, *Aiche J*, 1998, **44**, 405-415.